ARTICLE

A molecular boron cluster-based chromophore with dual emission

Kierstyn P. Anderson,[a] Mary A. Waddington,[a] Gary J. Balaich,[b] Julia M. Stauber,[a] Justin R. Caram,[a] Peter I. Djurovich,[c] and Alexander M. Spokoyny *[a]

Received 00th January 20xx,
Accepted 00th January 20xx

DOI: 10.1039/x0xx00000x

Bromination of the luminescent borane, *anti*-$B_{18}H_{22}$, via electrophilic substitution using $AlCl_3$ and Br_2, yields the monosubstituted derivative 4-Br-*anti*-$B_{18}H_{21}$ as an air-stable crystalline solid. In contrast to the unsubstituted parent compound, 4-Br-*anti*-$B_{18}H_{21}$ possesses dual emission upon excitation with UV light and exhibits fluorescence at 410 nm and phosphorescence at 503 nm, with Φ_{total} = 0.07 in oxygen-free cyclohexane. Increased oxygen content in cyclohexane solution quenches the phosphorescence signal. The fluorescent signal intensity remains unaffected by oxygen, suggesting that this molecule could be used as a ratiometric oxygen probe.

Introduction

Boron-containing luminescent molecules have been widely known and researched over decades for a variety of applications, including intracellular imaging,[1] sensors,[2] organic light emitting diodes[3] photovoltaics,[4] and lasers.[5] While the properties of molecules such as triarylboranes and borate-based dyes have received considerable attention, research into luminescent boron-rich hydride-based materials remains an underexplored field in which *closo*-dicarbadodecaboranes, also known as carboranes, have remained a central focus. This research has successfully developed emissive materials that incorporate carboranyl groups as components in metal complexes or luminescent polymers and oligomers.[3c, 6] However, due to the large band gap of carboranes (~8 eV), substitution onto the icosahedral cage is usually required for the molecule to participate in visible light transitions.[7] Consequently, a significant amount of work has focused on carborane functionalization methods.[8] In fact, only one known polyhedral borane to date, *anti*-$B_{18}H_{22}$, possesses inherent luminescence. This unique cluster best resembles two *nido*-$B_{10}H_{14}$ molecules fused at two vertices, forming an 18-vertex borane (Figure 1). Of the two known isomers of $B_{18}H_{22}$, *anti*-$B_{18}H_{22}$ and *syn*-$B_{18}H_{22}$, only the former is luminescent, featuring intense blue fluorescence at 407 nm when irradiated at 340 nm with a high quantum yield (Φ_{fluor} = 0.97).[9] Despite its discovery in 1962,[10] detailed analyses of luminescence from *anti*-$B_{18}H_{22}$ have only recently been described,[9,11] which found that both the HOMO and LUMO are distributed evenly across the boron cage. The absorbed energy in the S_1 state is redistributed

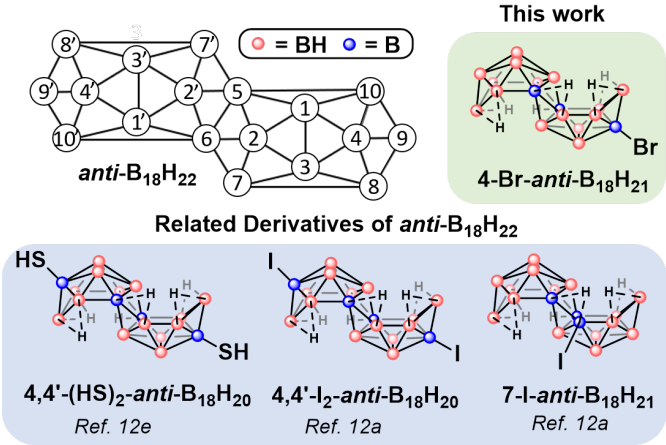

Figure 1: Top) Two-dimensional projection of *anti*-$B_{18}H_{22}$ and the brominated derivative discussed in this work. Bottom) Representations of select previously reported derivatives of *anti*-$B_{18}H_{22}$.

throughout the σ bonding framework resulting in a prolonged S_1 lifetime and, consequently, fluorescence.[9, 11] Since then, however, only a handful of synthetic derivatives of *anti*-$B_{18}H_{22}$ have been reported (Figure 1),[12] and a comprehensive synthetic foundation for this fascinating boron cluster system has yet to be established. From the existing reports it is clear that functionalization of the cluster dramatically alters its emissive properties.[10] For example, thiolation of the cluster gives 4,4'-$(HS)_2$-*anti*-$B_{18}H_{20}$, which displays red-shifted luminescence with fluorescent emission at 536 nm and phosphorescent emission at 597 nm.[12e] Reaction with pyridine yields a rearranged boron cage derivative, $B_{18}H_{20}(NC_5H_5)_2$, that exhibits thermochromic luminescence ranging from 585 nm (8 K) to 620 nm (300 K), which is caused by the constraint of the pyridine substituents at lower temperatures.[13] Most recently, the iodination of this cluster was reported, which described the green phosphorescence of both 7-I-*anti*-$B_{18}H_{21}$ and 4,4'-I_2-*anti*-$B_{18}H_{20}$ at 525 nm and 545 nm, respectively.[12a] Still, the relationship between $B_{18}H_{22}$ cluster structure and resulting photophysical properties has yet to be elucidated. It is therefore of great interest to explore

[a] Department of Chemistry and Biochemistry and California NanoSystems Institute (CNSI), University of California, Los Angeles, California 90095, United States
[b] Department of Chemistry and Chemistry Research Center, United States Air Force Academy, Colorado Springs, Colorado 80840, United States
[c] Department of Chemistry, University of Southern California, Los Angeles, California 90089, United States
Electronic Supplementary Information (ESI) available: [details of any supplementary information available should be included here]. See DOI: 10.1039/x0xx00000x

functionalization methods and investigate the effect that such changes have on the photoluminescence profile. Following the first account of halogenated *anti*-$B_{18}H_{22}$, we were interested in how other halogens affect the luminescent properties of this cluster. Herein we report a synthesis for the first brominated derivative of *anti*-$B_{18}H_{22}$, 4-Br-*anti*-$B_{18}H_{21}$, and its unique photophysical characteristics distinctively different from the other halogenated analogues.

Results and Discussion

Synthesis and Structural Characterization of 4-Br-*anti*-$B_{18}H_{21}$

Following conventional electrophilic bromination protocols used previously with other polyhedral boron clusters,[14] we treated *anti*-$B_{18}H_{22}$ with Br_2 (1 equiv) and $AlCl_3$ (15 mol%) in dichloromethane under an N_2 atmosphere at room temperature. Formation of the monobrominated cluster was observed after several hours, as suggested by an *in situ* mass spectrometry assay of the reaction mixture, although a significant amount of unreacted *anti*-$B_{18}H_{22}$ was still present after 18 hours. Increasing the amount of $AlCl_3$ (20 mol%) resulted in higher conversion to $B_{18}H_{21}Br$ with concomitant formation of the dihalogenated species, $B_{18}H_{20}Br_2$. Attempts to separate these two products were successful, but resulted in poor recovered yield of $B_{18}H_{21}Br$. Consequently, the procedure was further modified to improve the conversion to $B_{18}H_{21}Br$, which required fewer than 1 equiv of Br_2. These optimized conditions (15 mol% $AlCl_3$ and 0.70 equiv Br_2 in DCM) afforded a reaction mixture containing $B_{18}H_{22}$, $B_{18}H_{20}Br_2$, and $B_{18}H_{21}Br$ as major products as judged by *in situ* mass spectrometry analysis. Subsequently, $B_{18}H_{21}Br$ was purified from the crude mixture obtained from this reaction via high performance liquid chromatography (HPLC) using methanol/water mixture as an eluent on C-18 modified silica stationary phase,[15] giving a 22% yield. While the isolated material appeared pure by ^{11}B NMR spectroscopy, an impurity comprising ca. 5% of the bulk material was indicated by LC-MS analysis.

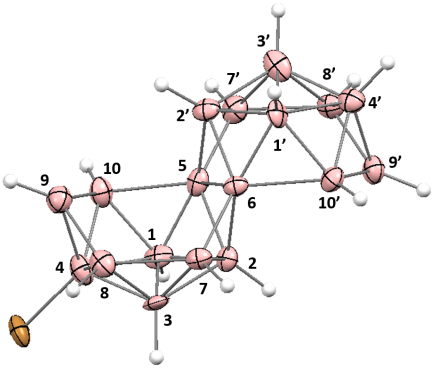

Figure 2: Single crystal X-ray structure of 4-Br-*anti*-$B_{18}H_{21}$•($2C_6H_6$) with labeled boron vertices. For clarity, the bridging hydrides, benzene solvent molecules are not shown. Displacement ellipsoids are drawn at a 50% probability level.

Consequently, further purification via HPLC was required to obtain >99% pure $B_{18}H_{21}Br$ as determined by LC-MS (see Figure S6, Table S1). The yield after the second purification was 8%. This product is stable when stored as a solid at 5°C.

Single crystal X-ray diffraction analysis was used to determine the structure of 4-Br-*anti*-$B_{18}H_{21}$. Single, X-ray quality colorless crystals of 4-Br-*anti*-$B_{18}H_{21}$ were grown by dissolution of the >95% pure compound in benzene followed by storage of the resulting solution at 5 °C (see SI). The resulting crystal structure indicated the possibility of co-crystallized impurities, $B_{18}H_{20}Br_2$ and $B_{18}H_{21}Cl$. The solid-state structure of 4-Br-*anti*-$B_{18}H_{21}$ (Figure 2) indicates that the boron atom connectivity in the cluster remains the same compared to the parent molecule, and that the bromine atom is located on the 4 position of the octadecaborane cage. Prior analyses of *anti*-$B_{18}H_{22}$[12a, 16] revealed that the 4 and 4' boron vertices are the most electron rich and therefore the most likely to undergo electrophilic substitution. Indeed, the doubly iodinated cluster, synthesized with I_2 and $AlCl_3$, is substituted at the 4 and 4' boron vertices.[12a] Therefore, electrophilic substitution of bromide at these locations is expected under the given experimental conditions. Even so, it is worthy to note that bromide substitution on vertices other than 4 and 4' was not indicated by other analytical methods including ^{11}B NMR spectroscopy. The selectivity of electrophilic substitution may consequently be a helpful synthetic tool in the exploration of *anti*-$B_{18}H_{22}$ chemistry.

Photophysical Properties

The absorption spectra of 4-Br-*anti*-$B_{18}H_{21}$ and *anti*-$B_{18}H_{22}$ are shown in Figure 3. Both compounds display transitions in the ultraviolet (UV) region with only minor changes in energy found for the lowest absorption bands in 4-Br-*anti*-$B_{18}H_{21}Br$ (λ_{max} = 300 nm and 343 nm) compared to *anti*-$B_{18}H_{22}$, (λ_{max} = 283 nm and 332 nm). However, the molar absorptivity of 4-Br-*anti*-$B_{18}H_{21}$ (ε_{342} = 1900 $M^{-1}cm^{-1}$) is significantly lower than that of *anti*-$B_{18}H_{22}$ (ε_{332} = 6800 $M^{-1}cm^{-1}$).

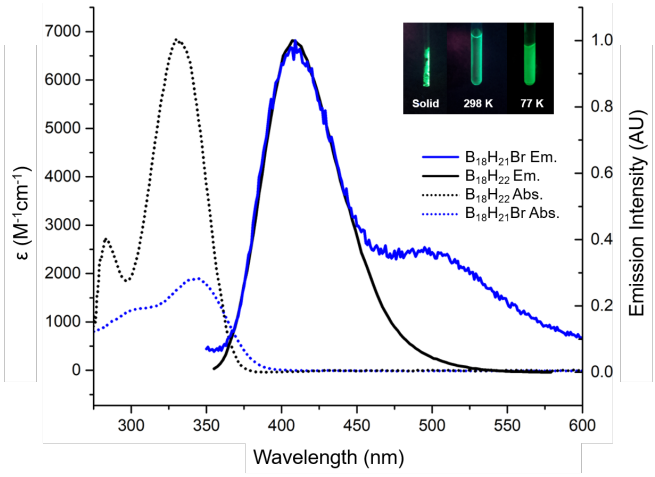

Figure 3: Absorption (dotted) and emission (solid) spectra of 4-Br-*anti*-$B_{18}H_{21}$ (blue) and *anti*-$B_{18}H_{22}$ (black). The wavelengths of excitation are 350 nm and 340 nm, respectively. All measurements were conducted in cyclohexane solution. Inset: Luminescence of 4-Br-*anti*-$B_{18}H_{21}$ in the solid state at 298 K and in hexanes at 298 K and 77 K.

Upon exposure to UV light, 4-Br-*anti*-$B_{18}H_{21}$ exhibits luminescence that is blue-green in a mixture of isomeric hexanes solution at room temperature and green when the solution is cooled to 77 K. Likewise, this green luminescence is present in the solid state (Figure 3, inset). Since *anti*-$B_{18}H_{22}$ is brightly fluorescent, we hypothesized that the bromide functionalized cluster would display some phosphorescent character due to the heavy atom effect.[17] The attached bromine would presumably enhance spin-orbit coupling (SOC) and improve spin-forbidden intersystem crossing (ISC) between singlet and triplet states that are close in energy. This permits the population of triplet states that may undergo radiative decay to produce phosphorescence. Intersystem crossing as it relates to SOC and the singlet-triplet energy gap is described by the equation

$$k_{ISC} \sim \frac{|\langle \Psi_{S1}|\mathcal{H}_{SO}|\Psi_{T1}\rangle|^2}{(\Delta E_{S1-T1})^2}$$

where $|\langle \Psi_{S1}|\mathcal{H}_{SO}|\Psi_{T1}\rangle|$ represents spin-orbit coupling and $\Delta E_{S1\text{-}T1}$ is the difference between the energies of the S_1 and T_1 states. Consequently, a smaller energy difference between the singlet and triplet states results in a large SOC value and more efficient intersystem crossing. To probe the possibility of phosphorescence, photophysical data of 4-Br-*anti*-$B_{18}H_{21}$ were first obtained under ambient conditions in cyclohexane. While the absorption spectra of *anti*-$B_{18}H_{22}$ and *anti*-$B_{18}H_{21}Br$ displayed in Figure 3 reveal slight differences in their λ_{max} values, the emission spectra exhibit more pronounced differences, with the brominated cluster displaying a shoulder at 503 nm. The variability in emission color, illustrated in Figure 3, prompted us to conduct more photoluminescence studies under various conditions. We suspected that the 503 nm shoulder observed could be phosphorescent in nature, but because room temperature phosphorescence is often difficult to observe the emission data were gathered at 77K. Under these conditions, bimolecular and diffusional quenching processes are minimized and molecular motions are restricted due to the molecule existing within a solid glass matrix.[18] With these pathways diminished, any occurring phosphorescence is likely to be detected. Indeed, at 77K the 503 nm peak is intense, nearly obscuring the 410 nm signal (Figure 4). To investigate the possibility of oxygen-quenched phosphorescence, the photophysical data in degassed (O_2-free) cyclohexane were gathered at 298 K. The emission spectrum shows the 410 nm peak and a considerably more intense 503 nm signal (Figure 4), indicating that oxygen is at least partially responsible for the low peak intensity initially observed.

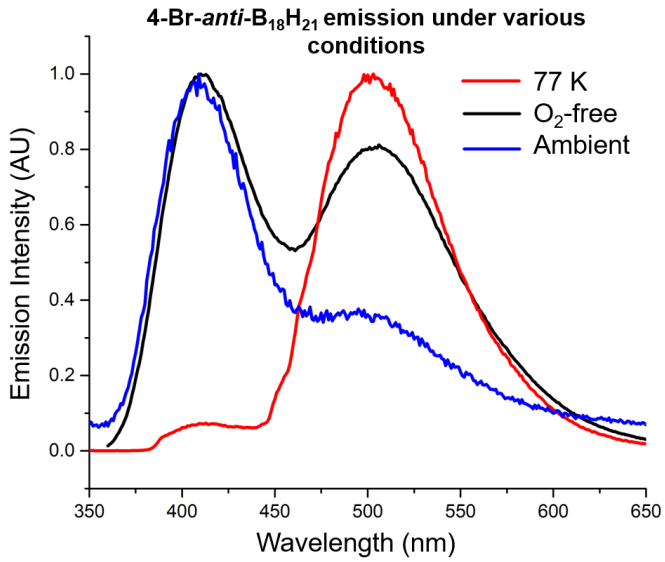

Figure 4: Emission spectra of 4-Br-*anti*-$B_{18}H_{21}$ in cyclohexane at 298 K under ambient conditions (blue), at 298 K in O_2-free cyclohexane (black), and at 77 K in methylcyclohexane (red). The wavelengths of excitation are 330 nm, 350 nm, and 340 nm, respectively.

The quantum yield (Φ) data, summarized in Table 1, also supports this hypothesis. Both cyclohexane solutions and PMMA films of 4-Br-*anti*-$B_{18}H_{21}$ possess smaller quantum yields when exposed to oxygen. The quantum yield of 4-Br-*anti*-$B_{18}H_{21}$ in cyclohexane under ambient conditions is 0.05, which increases to 0.07 when the measurement is conducted in oxygen-free solution. These low values are surprising considering that both iodinated clusters possess QY values no less than 0.41 in oxygen-free solution.[12a] The contribution to QY from fluorescence and phosphorescence (Φ_{fluor} and Φ_{phos}) was also determined (see Figures S9 and S10). Under ambient conditions in cyclohexane, both $\Phi_{fluor\text{-}amb}$ and $\Phi_{phos\text{-}amb}$ are 0.025, while in oxygen-free solution Φ_{fluor} = 0.024 and Φ_{phos} = 0.046. Because the fluorescence quantum yield remains the same within error for both conditions, the decrease in quantum yield from 0.07 to 0.05 is most

4-Br-*anti*-$B_{18}H_{21}Br$	emission λ_{max}	$\phi_{ambient}$	$\phi_{O2\text{-}free}$	τ (ns)	k_r 10^6 (s^{-1})	k_{nr} 10^6 (s^{-1})
Cyclohexane O_2-free[a]	503 410	-	0.07[a] 0.024/0.046[d]	11600[e] 10.3f[e]	0.0040[h] 2.3[i]	0.082[h] 95[i]
Cyclohexane[b]	410	0.05[b] 0.025/0.025[d]	-	10.6[f]	2.3[g]	92[g]
Methylcyclohexane[c]	503 407	-	-	552000[e] 9.8[f]	- -	- -

Table 1: Summary of photophysical properties of 4-Br-*anti*-$B_{18}H_{21}$. [a]Collected at 298 K under N_2 atmosphere. [b]Collected at 298 K under ambient conditions. [c]Collected at 77 K. [d]Quantum efficiency of fluorescence (ϕ_{fluor})/Quantum efficiency of phosphorescence (ϕ_{phos}), calculated by multiplying peak percent by the quantum yield of the cyclohexane solution under ambient or O_2-free conditions (Figures S9 and S10). [e]Obtained by exciting at 372 nm and observing at 525 nm. [f]Obtained by exciting at 331 nm and observing at 410 nm. Error in the excited state lifetime measurement is ±14% and ±10%, respectively. [g,h,i]Calculated according to the equations $k_r = \phi/\tau$ and $k_{nr} = (1 - \phi)/\tau$, where k_r is the radiative rate constant, k_{nr} is the nonradiative rate constant, ϕ is the quantum efficiency under ambient conditions ($\phi_{ambient}$),[g] of ϕ_{phos} under N_2,[h] or ϕ_{fluor} under N_2,[i] and τ is the excited state lifetime.

likely due to oxygen-quenched phosphorescence. The quantum yield of a 4-Br-*anti*-$B_{18}H_{21}$ PMMA film was also assessed, increasing from <0.01 to 0.08 when under N_2, which is similar with the low values of the solid-state iodinated clusters (0.06 for 7-I-*anti*-$B_{18}H_{21}$ and 0.11 for 4,4'-I_2-*anti*-$B_{18}H_{20}$).[12a] Because diffusion of oxygen at room temperature in PMMA is significantly slower than in cyclohexane, the system was allowed to equilibrate under the flow of O_2 for over 30 minutes (see Figure S8).[19] Finally, the fluorescent and phosphorescent nature of these peaks were further explored through lifetime (τ) decay experiments. For a cyclohexane solution of 4-Br-*anti*-$B_{18}H_{21}$, the 410 nm peak lifetime is 10.6 ns under ambient conditions (Table 1, Figure S11), compared to that of the parent borane (11.2 ns).[9] This value remains consistent under oxygen-free atmosphere (τ = 10.3 ns) and decreases slightly at 77 K (τ = 9.8 ns). The lifetime decay data was also gathered for the 503 nm peak, revealing a lifetime of 11.6 µs in oxygen-free cyclohexane at 298 K. At 77 K, the lifetime is extended dramatically (τ = 552 µs) (Table 1, Figure S11), which further supports the photoluminescence data in Figure 4. The photoluminescence, quantum yield, and lifetime data for 4-Br-*anti*-$B_{18}H_{21}$ under the conditions studied are summarized in Table 1. This data can be further contextualized through a comparison to the other reported monohalogenated derivative, 7-I-*anti*-$B_{18}H_{21}$.[12a] The iodinated cluster contains only a single emission peak that is attributed to phosphorescence, which is probably due to the increased singlet and triplet state overlap that results from the heavy iodine atom.[12a, 20] The monobrominated cluster displays attenuated ISC in comparison, achieving a balance between singlet and triplet states that permits dual fluorescent/phosphorescent emission.

The simultaneous fluorescence and oxygen-sensitive phosphorescence demonstrated by 4-Br-*anti*-$B_{18}H_{21}$ is a property not commonly observed by small molecule metal-free emitters.[20] Although dual emission was reported for thiolated *anti*-$B_{18}H_{22}$, the two luminescence bands in this molecule overlap significantly, obscuring small changes in the oxygen-sensitive phosphorescence signal.[10e] In contrast, the energy difference between the two emission events for 4-Br-*anti*-$B_{18}H_{21}$ is large enough that the fluctuating intensity of the phosphorescence peak is easily observed. These combined characteristics make the 4-Br-*anti*-$B_{18}H_{21}$ chromophore potentially useful for oxygen sensing. Emissive oxygen

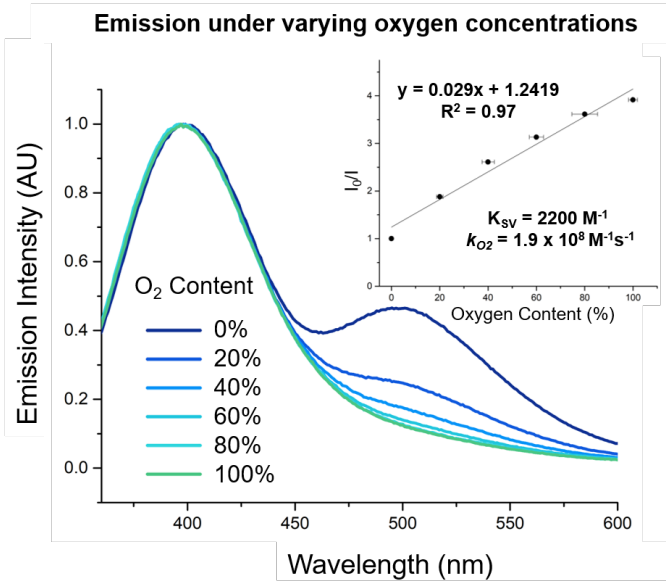

Figure 5: Emission spectra of 4-Br-*anti*-$B_{18}H_{21}$ in cyclohexane degassed with N_2 and O_2 gas mixtures containing varying amounts of oxygen. The wavelength of excitation was 320 nm. Inset) Stern-Volmer plot of phosphorescence quenching of the 503 nm peak. The quenching constant K_{SV} and bimolecular rate constant of T_1 state quenching k_q were calculated using 0.00116 mole fraction atm^{-1} as the solubility of O_2 in cyclohexane[24] and the Stern-Volmer equation: $I^0/I = 1+K_{SV}[O_2]$, $K_{SV} = k_{O2}\tau_0$.

sensors have been intensely studied due to their wide applicability in biological imaging.[21] Although oxygen can be detected and measured based on a single emission signal, a ratiometric probe based on dual-emissivity is more reliable due to the presence of a reference signal. Many dual-emitting sensors are nanoparticle or heavy-metal based, or require the combination of two different luminophores (one fluorescent, the other phosphorescent).[20] This is due to the difficulty involved in rationally designing a single dual-emitting small molecule with the appropriate balance of populated singlet and triplet states that would give rise to dual emission. This phenomenon is especially difficult to achieve with entirely organic systems, and most dual-emissive organic small molecules are based on polycyclic aromatic molecules such as pyrene[22] or naphthalene.[23] However, each of these methods are accompanied by a host of disadvantages, such as unequal stability between mixed dyes, weak phosphorescence, photobleaching, and bio-incompatibility. The ideal ratiometric

	State Transition	Composition	λ_{VA} or λ_{VE} (nm)	*f*
Excitation	$S_0 \rightarrow S_1$	HOMO → LUMO	357	0.0443
		HOMO-1 → LUMO	347	0.0336
		HOMO-2 → LUMO	288	0.0909
Emission	$S_0 \rightarrow S_1$	HOMO → LUMO	374	-
	$S_0 \rightarrow T_1$	HOMO → LUMO	487	-

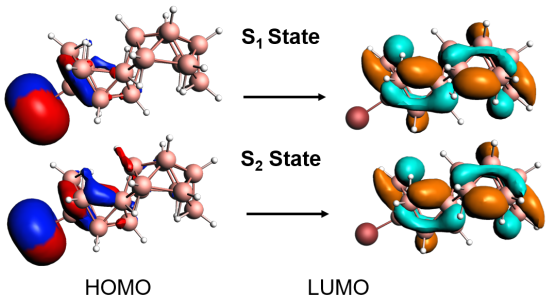

Figure 6: Left) Summary of relevant calculated absorption and emission spectra (Hybrid PBE0 DZP) for 4-Br-*anti*-$B_{18}H_{21}$, where λ_{VA} is the calculated vertical absorption wavelength, λ_{VE} is the calculated vertical emission wavelength, *f* is the oscillator strength, and λ_{max} is the corresponding experimental wavelength. Excitation calculations were based on the S_0 optimized geometry and emission calculations were based on the S_1, S_2 or T_1 optimized geometries. Right) Natural Transition Orbitals (NTOs) for the electronic transitions of the S_1 and S_2 states. The remaining relevant NTOs are shown in Figure S14.

oxygen probe exhibits intense oxygen-sensitive phosphorescence, long lifetime, resistance to photobleaching, and stability.[20] To assess the applicability of 4-Br-*anti*-$B_{18}H_{21}$ as a small molecule oxygen sensor, preliminary sensing studies were conducted. Mixtures of nitrogen and oxygen gas containing varying amounts of oxygen were bubbled through a cyclohexane solution of 4-Br-*anti*-$B_{18}H_{21}$ before measurements were conducted (see Table S4). As shown in Figure 5, phosphorescence decreases significantly with increasing oxygen content while the fluorescence peak maintains its intensity. This system functions as a ratiometric probe through comparison of the reference signal (the oxygen-insensitive fluorescence peak) to the intensity of the oxygen-quenchable phosphorescence peak. The intermolecular, collisional quenching process by oxygen follows Stern-Volmer kinetics (see inset of Figure 5). Using a previously reported value for the solubility of oxygen in cyclohexane[24] and the Stern-Volmer relationship, the Stern-Volmer quenching constant was calculated, K_{SV} = 2200 M^{-1} along with the bimolecular rate quenching constant, k_{O2} = 1.9 x 10^8 $M^{-1}s^{-1}$. The latter value can be directly compared to the quenching rate of 7-I-*anti*-$B_{18}H_{21}$ (4.1 x 10^7 $M^{-1}s^{-1}$) and 4,4'-I_2-*anti*-$B_{18}H_{20}$ (6.8 x 10^7 $M^{-1}s^{-1}$).[12a] It is evident that oxygen quenching occurs an order of magnitude faster in the brominated borane than its iodinated counterparts. Finally, the electrochemical properties of both *anti*-$B_{18}H_{22}$ and 4-Br-*anti*-$B_{18}H_{21}$ were assessed through cyclic voltammetry (see Figure S12). Both compounds exhibit an irreversible reduction, with a potential that shifts cathodically from -1.36 V (*anti*-$B_{18}H_{22}$) to -1.18 V (4-Br-*anti*-$B_{18}H_{21}$) vs the ferrocene couple at 0 V Fc^+/Fc.

DFT Analysis of Photophysical Data

As a supplement to experimental data, computational calculations were conducted using TD-DFT on ADF software. A DFT hybrid PBE0 functional and DZP basis set was used with scalar relativistic effects considered. Optimized geometry coordinates and frequency calculations can be found in Tables S6-9. First, the absorption spectrum was calculated based on the optimized singlet ground state geometry, S_0. As shown in Figure 6, three vertical absorption (λ_{VA}) events with oscillator strengths > 0.02 occur between 290-350 nm, the approximate range in which the molecule was excited in the photoluminescence experiments. While these transitions originate from the HOMO (-8.31 eV), HOMO-1 (-8.42 eV), or HOMO-2 (-9.18 eV), they are all singlet-singlet processes that excite into the LUMO (-4.09 eV). Importantly, there are two calculated bands at 347 nm and 357 nm that correspond to the broad experimental band at 343 nm. The relatively small oscillator strengths for these transitions (~3-4 times smaller than those of *anti*-$B_{18}H_{22}$, Table S5), are in accordance with the absorption spectrum and ε values in Figure 3. The emission spectrum, based on the optimized geometry of the S_1 state, was calculated, resulting in a vertical emission wavelength (λ_{VE}) at 374 nm, which best corresponds to the experimental λ_{max} at 410 nm. In order to determine the origin of phosphorescence, the T_1 optimized geometry was calculated. The energy difference between the S_1 and T_1 states is 0.22 eV, a relatively small gap in which intersystem crossing would be possible. Therefore, phosphorescence will most likely occur from the T_1 state. The emission spectrum based on the optimized geometry of the T_1 state was calculated, giving λ_{VE} = 487 nm, which matches well with the experimental band maximum λ_{max} = 503 nm. The natural transition orbitals (NTOs) for the S_1, and S_2 states are shown in Figure 7, whereas the NTO for the T_1 state, which is similar to the S_1 state, is included in Figure S14. The NTOs show that the HOMO for S_1 and S_2 states have predominantly bromine p-orbital (n_{Br}) character. Furthermore, the bromine p-orbital in the S_2 state is orthogonal to the S_1 state, which will consequently favor SOC and therefore ISC. This feature is consistent with the fast ISC process observed in the experimental lifetime decay experiments. All of these excited states have a common LUMO, which is distributed exclusively on the boron cluster. Therefore, while fluorescence from the parent borane can be characterized as a $^1(\sigma \rightarrow \sigma^*)$ transition involving B-B and B-H bonds (Figure S13), emission from 4-Br-*anti*-$B_{18}H_{21}$ can be assigned to $^1(n_{Br} \rightarrow \sigma^*)$ and $^3(n_{Br} \rightarrow \sigma^*)$ charge transfer transitions, which would presumably contribute to the efficient ISC in this system.

Conclusions

This work presents the synthesis and photophysical characterization of the dually emissive *anti*-$B_{18}H_{21}Br$ molecule, which was prepared from *anti*-$B_{18}H_{22}$ through electrophilic substitution with $AlCl_3$ and Br_2. This molecule is a rare example of a boron-based dual emitting chromophore. Its simultaneous fluorescence and phosphorescence originate from a delicate balance of S_1 and T_1 state population afforded by the bromo substituent. While the phosphorescence is quenched by oxygen, the fluorescence signal maintains its intensity, suggesting that this molecule could be useful as a ratiometric oxygen probe. The synthesis of 4-Br-*anti*-$B_{18}H_{21}$ offers a contribution to the synthetic toolbox for *anti*-$B_{18}H_{22}$, while also elucidating the relationship between cluster structure and photophysical properties. More broadly, this work presents further advances in the burgeoning field of boron-containing luminescent and photoactive materials.[25]

Conflicts of interest

There are no conflicts of interest to declare.

Acknowledgements

This work was supported by NSF Grants CHE-1846849 (NSF CAREER Award to A.M.S.) and DGE-1650604 (NSF GRFP for K.P.A.). We thank Mr. Nicholas Bernier (UCLA) for assisting with the oxygen sensing studies and Boron Specialties for a generous gift of $B_{18}H_{22}$.

References

1 (a) T. Kowada, H. Maeda, K. Kikuchi, *Chem. Soc. Rev.*, 2015, **44** (14), 4953. (b) A. Sutter, M. Elhabiri, G. Ulrich, *Chem. Eur. J.* 2018, **24**, 11119.

2 (a) K. Rurack, M. Kollmannsberger, J. Daub, *Angew.*, 2001, **40** (2), 385; (b) S. Yamaguchi, S. Akiyama, K. Tamao, *J. Am. Chem. Soc.*, 2001, **123** (46), 11372. (c) S. K. Mellerup, S. Wang, *Chem. Soc. Rev.* 2019, **48**, 3537.

3 Recent select examples (see references within): (a) K. S. Mellerup and S. Wang, Trends in Chem. 2019, **1** (1), 77. (b) J. Lei, S. Griesbeck, T. B. Marder, *Chem. Sci.* 2017, **8**, 846. (c) K. O. Kirlikovali, J. C. Axtell, A. Gonzalez, A. C. Phung, S. I. Khan, A. M. Spokoyny, *Chem. Sci.*, 2016, **7** (8), 5132.

4 (a) S. Yruegas, J. J. Martinez, C. D. Martin, *Chem. Comm.*, 2018, **54** (50), 6808; (b) T. C. Li, F. Fabregat-Santiago, O. K. Farha, A. M. Spokoyny, S. R. Raga, J. Bisquert, C. A. Mirkin, T. J. Marks, J. T. Hupp, *J. Phys. Chem. C* 2011, **115** (22), 11257.

5 R. T. Kuznetsova, Y. V. Aksenova, E. N. Tel'minov, L. G. Samsonova, G. V. Maier, T. N. Kopylova, S. L. Yutanova, E. V. Antina, M. B. Berezin, G. B. Guseva, *Opt. Spectrosc.*, 2012, **112** (5), 746.

6 (a) B. P. Dash, R. Satapathy, E. R. Gaillard, J. A. Maguire, N. S. Hosmane, *J. Am. Chem. Soc.*, 2010, **132** (18), 6578. (b) S. Mukherjee, P. Thilagar, *Chem. Comm.*, 2016, **52** (6), 1070; (c) K. Kokado, Y. Tokoro, Y. Chujo, *Macromolecules*, 2009, **42** (8), 2925.

7 R. N. Grimes, *Carboranes, 3rd ed.* Academic Press: 2016.

8 Representative examples (see references within): (a) R. Núñez, M. Tarrés, A. Ferrer-Ugalde, F. F. de Biani, F. Teixidor, *Chem. Rev.*, 2016, **116** (23), 14307; (b) Y. Quan, Z. Xie, *Chem. Soc. Rev.*, 2019, **48** (13), 3660; (c) S. P. Fisher, A. W. Tomich, S. O. Lovera, J. F. Kleinsasser, J. Guo, M. J. Asay, H. M. Nelson, V. Lavallo, *Chem. Rev.,* 2019, **119** (14), 8262.

9 M. G. S. Londesborough, D. Hnyk, J. Bould, L. Serrano-Andrés, V. Sauri, J. M. Oliva, P. Kubát, T. Polívka, K. Lang, *Inorg. Chem.*, 2012, **51** (3), 1471.

10 A. R. Pitochelli, M. F. Hawthorne, *J. Am. Chem. Soc.*, 1962, **84** (16), 3218.

11 L. Cerdán, J. Braborec, I. Garcia-Moreno, A. Costela, M. G. S. Londesborough, *Nat. Commun.*, 2015, **6**, 5958.

12 (a) M. G. S. Londesborough, J. Dolanský, J. Bould, J. Braborec, K. Kirakci, K. Lang, I. Císařová, P. Kubát, D. Roca-Sanjuán, A. Francés-Monerris, L. Slušná, E. Noskovičová, D. Lorenc, *Inorg. Chem.*, 2019, **58** (15), 10248; (b) M. G. S. Londesborough, J. Dolanský, T. Jelínek, J. D. Kennedy, I. Císařová, R. D. Kennedy, D. Roca-Sanjuán, A. Francés-Monerris, K. Lang, W. Clegg, *Dalton Trans.,* 2018, **47** (5), 1709; (c) M. G. S. Londesborough, R. Macías, J. D. Kennedy, W. Clegg, J. Bould, *Inorg. Chem.*, 2019, **58** (19), 13258; (d) R. L. Sneath, L. J. Todd, *Inorg. Chem.*, 1973, 12 (1), 44; (e) V. Saurí, J. M. Oliva, D. Hnyk, J. Bould, J. Braborec, M. Merchán, P. Kubát, I. Císařová, K. Lang, M. G. S. Londesborough, *Inorg. Chem.*, 2013, **52** (16), 9266.

13 M. G. S. Londesborough, J. Dolanský, L. Cerdán, K. Lang, T. Jelínek, J. M. Oliva, D. Hnyk, D. Roca-Sanjuán, A. Francés-Monerris, J. Martinčík, M. Nikl, J. D. Kennedy, *Adv. Opt. Mater.*, 2017, **5** (6), 1600694.

14 R. M. Dziedzic, L. M. Saleh, J. C. Axtell, J. L. Martin, S. L. Stevens, A. T. Royappa, A. L. Rheingold, A. M. Spokoyny, *J. Am. Chem. Soc.*, 2016, **138** (29), 9081.

15 L. C. Sander, S. A. Wise, S. A., *Anal. Chem.* 1984, **56** (3), 504.

16 P. G. Simpson, W. N. Lipscomb, *J. Chem. Phys.*, 1963, **39** (1), 26.

17 K. N. Solov'ev, E. A. Borisevich, *Physics-Uspekhi* 2005, **48** (3), 231.

18 N. J. Turro, V. Ramamurthy, J. C. Scaiano, *Principles of molecular photochemistry : an Introduction*. University Science Books: 2009.

19 (a) I. M. Krieger, G. W. Mulholland, C. S. Dickey, *J. Phys. Chem.*, 1967, **71** (4), 1123; (b) E. I. Hormats, F. C. Unterleitner, *J. Phys. Chem.*, 1965, **69** (11), 3677; (c) H. Y. Kaptan, *J. Appl. Polym. Sci.*, 1999, **71** (7), 1203.

20 Y. Feng, J. Cheng, L. Zhou, X. Zhou, H. Xiang, *Analyst*, 2012, **137** (21), 4885.

21 Y. Zhao, L. Liu, T. Luo, L. Hong, X. Peng, R. H. Austin, J. Qu, *Sensor. Actuat. B- Chem.*, 2018, **269**, 88.

22 B. J. Basu, A. Thirumurugan, A. R. Dinesh, C. Anandan, K. S. Rajam, *Sensor. Actuat. B- Chem.*, 2005, **104** (1), 15.

23 E. D. Lee, T. C. Werner, W. R. Seitz, *Anal. Chem.*, 1987, **59** (2), 279.

24 J. D. Wild, T. Sridhar, O. E. Potter, *Chem. Eng. J.,* 1978, **15** (3), 209.

25 Key representative examples (see references within): (a) X. Li, Y. Shi, N. Wang, T. Peng, S. Wang, *Chem. Eur. J.,* 2019, **25**, 5757; (b) L. Dong, F. Saraci, K. Yuan, X. Wang, S. Wang, *Org. Biomol. Chem.,* 2019, **21** (26), 6470; (c) M. Ito, E. Ito, M. Hirai, S. Yamaguchi, *J. Org. Chem.*, 2018, **83** (15), 8449; (d) C. D. Entwistle, T. B. Marder, *Chem. Mater.*, 2004, **16** (23), 4574; (e) X. Jia, J. Nitsch, L. Ji, Z. Wu, A. Friedrich, F. Kerner, M. Moos, C. Lambert, T. B. Marder, *Chem. Eur. J.*, 2019, **25** (46), 10845; (f) M. Vanga, R. A. Lalancette, F. Jäkle, *Chem. Eur. J.*, 2019, **25** (43), 10133; (g) K. Liu, R. A. Lalancette, F. Jäkle, *J. Am. Chem. Soc.*, 2019, **141** (18), 7453; (h) M. Gorbe, A. M. Castro, F. Sancenón, R. Martínez-Máñez, R. Ballesteros-Cillero, L. E. Ochando, K. Chulvi, R. Gotor, S. Gil, *Dyes Pigm.,* 2019, **160**, 198; (i) C. Ray, C. Schad, E. Avellanal-Zaballa, F. Moreno, J. Bañuelos, B. L. Maroto, S. de la Moya, *Proceedings*, 2019, **41** (1), 54; (j) Z. Domíngez, V. F. Paid, D. Collado, P. Vázquez-Domínguez, F. A. Albendín, A. Pérez-Inestrosa, A. Ros, U. Pischel, *J. Org. Chem.*, 2019, **84** (21), 13384. (k) J. S. Ishibashi, C. Darrigan, A. Chrostowska, B. Li, S.-Y. Liu, *Dalton Trans.*, 2019, **48** (8), 2807. (l) D. Jung, L. M. A. Saleh, Z. J. Berkson, M. F. El-Kady, J. Y. Hwang, N. Mohamed, A. I. Wixtrom, E. Titarenko, Y. Shao, K. Mccarthy, J. Guo, I. B. Martini, S. Kraemer, E. C. Wegener, P. Saint-Cricq, B. Ruehle, R. R. Langeslay, M. Delferro, J. L. Brosmer, C. H. Hendon, M. Gallagher-Jones, J. Rodriguez, K. W. Chapman, J. T. Miller, X. Duan, R. B. Kaner, J. I. Zink, B. F. Chmelka, A. M. Spokoyny, *Nature Mater.* 2018, **17**, 341. (m) J. C. Axtell, M. S. Messina, J.-Y. Liu, D. Galaktionova, J. Schwan, T. M. Porter, M. D. Savage, A. I. Wixtrom, A. L. Rheingold, C. P. Kubiak, J. R. Winkler, H. B. Gray, P. Kral, A. N. Alexandrova, A. M. Spokoyny, *Inorg. Chem.* 2019, **58** (16), 10516, (n) H. L. van de Wouw, R. S. Klausen, *J. Org. Chem*. 2019, **84** (3), 1117.